Effective Characterization of Fractured Media with PEDL: A Deep Learning-Based Data Assimilation Approach

Tongchao Nan[1, 2], Jiangjiang Zhang[1, 2*], Yifan Xie[3], Chenglong Cao[1, 2], Jichun Wu[4], and Chunhui Lu[1, 2, 3, 5]

[1] Yangtze Institute for Conservation and Development, Hohai University, Nanjing, China,

[2] The National Key Laboratory of Water Disaster Prevention, Hohai University, Nanjing, China,

[3] College of Water Conservancy and Hydropower Engineering, Hohai University, Nanjing, China,

[4] Key Laboratory of Surficial Geochemistry of Ministry of Education, School of Earth Sciences and Engineering, Nanjing University, Nanjing, China,

[5] College of Hydrology and Water Resources, Hohai University, Nanjing, China.

Corresponding Author: Jiangjiang Zhang (zhangjiangjiang@hhu.edu.cn)

Key Points

- A deep learning-based data assimilation method, named PEDL, is proposed to characterize fractured media with highly non-Gaussian features.
- PEDL outperforms three popular data assimilation methods based on deep learning or the Kalman formula.
- Sensitivity analyses confirm PEDL's validity and adaptability across various ensemble sizes and DL model architectures.

Abstract

In various research fields such as hydrogeology, environmental science and energy engineering, geological formations with fractures are frequently encountered. Accurately characterizing these fractured media is of paramount importance when it comes to tasks that demand precise predictions of liquid flow and the transport of solute and energy within them. Since directly measuring fractured media poses inherent challenges, data assimilation (DA) techniques are typically employed to derive inverse estimates of media properties using observed state variables like hydraulic head, concentration, and temperature. Nonetheless, the considerable difficulties arising from the strong heterogeneity and non-Gaussian nature of fractured media have diminished the effectiveness of existing DA methods. In this study, we formulate a novel DA approach known as PEDL (parameter estimator with deep learning) that harnesses the capabilities of DL to capture nonlinear relationships and extract non-Gaussian features. To evaluate PEDL's performance, we conduct two numerical case studies with increasing complexity. Our results unequivocally demonstrate that PEDL outperforms three popular DA methods: ensemble smoother with multiple DA (ESMDA), iterative local updating ES (ILUES), and ES with DL-based update (ESDL). Sensitivity analyses confirm PEDL's validity and adaptability across various ensemble sizes and DL model architectures. Moreover, even in scenarios where structural difference exists between the accurate reference model and the simplified forecast model, PEDL adeptly identifies the primary characteristics of fracture networks.

1 Introduction

Fractures are narrow openings or mechanical discontinuities in geological formations, typically found in rocks, soils, and aquifers. The significance of fractures lies in their pivotal role across numerous processes: they offer preferential pathways for the rapid transport of liquids, and act as reservoirs for fluid storage and release (Viswanathan et al., 2022). Despite their relatively minor presence within the subsurface media, fractures hold importance in diverse fields, including Karst aquifer management (S Li et al., 2020), geothermal energy production (Guo et al., 2022), hydrocarbon extraction (F Zhang & Emami-Meybodi, 2022), geological sequestration of CO_2 (Luo et al., 2022), and nuclear waste disposal (Saceanu et al., 2022). Nonetheless, the complexity

of fractured media is deeply ingrained in the coexistence of fractures with varying sizes, orientations, and apertures. This complexity engenders significant heterogeneity, anisotropy, and discontinuity in the hydraulic characteristics of fractured media, ultimately giving rise to elevated levels of uncertainty in flow and transport predictions (Neuman, 2005). For achieving trustworthy process comprehension and simulation outcomes, it is imperative to effectively characterize the attributes of fractured media and reasonably quantify the associated uncertainty (Hyman, 2020; Klepikova et al., 2020).

Given the inherently opaque and complex nature of fractured media, the direct observation of fractures poses a formidable challenge. Although X-ray computed tomography can be employed to study the structure of fracture in specific scenarios, it is subject to limitations related to method resolution and sample size (C Jiang et al., 2019; Hao Wu et al., 2019). An alternative approach to characterizing fractured media involves the use of numerical models that explicitly represent fracture networks, particularly the major ones (Berre et al., 2019). These models, often referred to as discrete fracture models (DFMs), encompass a range of methodologies, including channel networks (Hyman, 2020), discrete fracture networks (Cacas et al., 1990), discrete fracture-matrix models (Koohbor et al., 2020), and embedded discrete fracture-matrix (EDFM) models (J Jiang & Younis, 2017). To characterize the inherent structural complexity and scale disparities within fracture networks, it is often imperative to employ fine spatial resolutions. Nevertheless, this approach can make simulations prone to griding failures, result in high computational expenses, and, as a consequence, prove infeasible for extensive, large-scale problems (Viswanathan et al., 2022). A simpler yet less precise approach for representing fractures involves utilizing continuum models, where effective parameter values of the matrix are employed. These models include the stochastic continuum (SC) model (Tsang et al., 1996) and the dual-permeability model (Presho et al., 2011). While these models may not provide the same level of accuracy as DFMs, they are known for their ease of implementation and cost-effectiveness in practical applications (National Academies of Sciences, 2020).

In the aforementioned models, a substantial number of parameters are indispensable for representing complex fractures. However, these parameters remain predominantly unknown, introducing considerable uncertainty when simulating flow and transport processes happening within the fractured media. To confront this challenge, researchers have underscored the growing importance of incorporating diverse data types, encompassing hydraulic, geophysical, and hydro-

chemical measurement data, through the implementation of data assimilation (DA) techniques (Elahi & Jafarpour, 2018; Y Li et al., 2016; Miskimins, 2009; Ping & Zhang, 2013; Hui Wu et al., 2021). DA is devoted to seamlessly integrating theoretical knowledge, often represented as numerical models, with observational data to achieve optimized estimations of system states, parameters, and initial/boundary conditions. It has found extensive applications across various research domains of geosciences (Carrassi et al., 2018; Fletcher, 2022), and can serve as a valuable tool for enhancing our understanding of fractures and their properties.

When characterizing fractured media, the prevailing DA approach in use is ensemble Kalman filter (EnKF) (Evensen, 2009) and its iterative variations, such as ESMDA (Emerick & Reynolds, 2013) and EnRML (Gu & Oliver, 2007). For instance, Vogt et al. (2012) employed EnKF to assimilate tracer data, aiming to estimate equivalent permeability field of discrete fracture networks at an enhanced geothermal system reservoir. However, their predictions display a noticeable degree of uncertainty, which could be attributed to the inherent constraints of EnKF and its variants in handling non-Gaussian distributions. To tackle this challenge, a viable strategy involves transforming non-Gaussian distributed variables into Gaussian ones using various techniques. For example, Hui Wu et al. (2021) applied principal component analysis, Chen et al. (2023) used deep generative model, Ping & Zhang (2013) utilized level set function, and Lu & Zhang (2015) employed Hough transformation, respectively, to reparameterize complex fractured media with Gaussian random variables. These Gaussian distributed variables can be effectively updated using EnKF or its variants, and then transformed back to non-Gaussian distributed fracture parameters to make predictions with dynamic models. Nevertheless, it's important to note that the reparameterization and updating processes may lead to the loss of some basic features and continuity of fractures (Yao et al., 2018). Another strategy for addressing the non-Gaussianity issue entails adopting more theoretically robust DA methods, such as Markov chain Monte Carlo (MCMC) (Vrugt, 2016) and particle filter (PF) (Djuric et al., 2003). For example, Blaheta et al. (2020) and Xue et al. (2020) respectively employed MCMC and PF for the characterization of fractured media in subsurface applications. Nevertheless, the computational costs associated with MCMC and PF can become prohibitive when dealing with high-dimensional inverse problems. Even with the incorporation of lower-fidelity or surrogate models to improve efficiency in the two studies, the practical application of MCMC and PF techniques remains a formidable challenge. In addition to the challenge posed by non-

Gaussianity, another prevalent and complex issue in the realm of DA for subsurface characterization is equifinality, which refers to the scenario where various model structures and parameter combinations can yield acceptable reproductions of observed system behaviors (Beven & Freer, 2001). From the Bayesian perspective, equifinality means that the parameter distribution is multi-modal in ensemble sense. Several studies have tried to handle multi-modal distributions in DA by conceptualizing them as a mixture of Gaussian distributions, with each of these distributions being updated individually (Elsheikh et al., 2013; Sun et al., 2009; J Zhang et al., 2018). Among them, the iterative local updating ensemble smoother (ILUES) proposed by J Zhang et al. (2018) has been used as the basic DA method in various subsurface characterization problems.

Over the past decade, deep learning (DL) has gained substantial attention within the field of hydrology and water resources (Shen, 2018). DL's prowess in unveiling complex nonlinear relationships and intricate patterns from data has endowed it with formidable analytical capabilities. Moreover, the strong alignment between DL and DA in terms of statistical principles and methodologies has been well investigated and recognized (Abarbanel et al., 2018; Berry & Harlim, 2017). In an effort to tackle the challenges posed by high-dimensionality and non-Gaussianity in DA problems, J Zhang et al. (2020) put forth an innovative approach. They proposed the utilization of DL to establish a nonlinear updating scheme that supplants the conventional Kalman updating in EnKF and its variants. Their findings showcased the efficacy of this DL-based DA method, known as ESDL, in effectively characterizing high-dimensional, non-Gaussian parameter fields. Due to its capability to address complex DA problems, ESDL and its variants have found applications in numerous subsurface characterization scenarios (Godoy et al., 2022; Man et al., 2022; Wang & Yan, 2022; Xiao et al., 2023; J Zhang et al., 2023).

In the present study, we adopt the ESDL method for the first time to characterize fractured media. While ESDL exhibits improved performance compared to Kalman-based DA methods like ESMDA and ILUES, it is not without its limitations, as will be demonstrated later in this work. The fracture networks inferred by ESDL exhibit some irregularities, possibly due to the updating process from the innovation vector (i.e., the difference between observations and model predictions) to the update vector (i.e., the difference between posterior and prior parameters). Based on this finding, we improve ESDL by introducing a new updating rule. This new DA

method, named parameter estimator with DL (PEDL), establishes a direct update from the multi-sourced observation vector to the posterior parameter vector. To validate PEDL's effectiveness, we compare its performance with several existing DA methods, including ESMDA, ILUES, and ESDL, in a groundwater flow problem within fractured media. As will be demonstrated later, PEDL outperforms the other three DA methods significantly in characterizing the fractured media.

The rest of this paper is structured as follows. In Section 2, we present the implementation details of PEDL, along with three well-known DA methods for comparative analysis, namely ESMDA, ILUES, and ESDL. Section 3 features two illustrative cases aimed at evaluating the performance of PEDL in the context of DA within fractured media. Here, we consider two scenarios with and without considering the model structural error, respectively. Finally, in Section 4, we draw conclusions and engage in a discussion about the applicability of PEDL in a broader perspective.

2 Methodology

Here, we assume that the process of concern (e.g., groundwater flow within a fractured aquifer) is simulated by a numerical model $\mathcal{F}(\mathbf{m})$. The true parameters $\mathbf{m}^*$ describing the media properties (e.g., permeability) are unknown and can be inferred from noisy measurement data

$$\tilde{\mathbf{d}} = \mathcal{F}(\mathbf{m}^*) + \boldsymbol{\varepsilon}, \tag{1}$$

where $\boldsymbol{\varepsilon} \sim \mathcal{N}(\mathbf{0}, \mathbf{C}_\mathrm{D})$ represent the error terms. Based on the Bayesian theory, our updated understanding about the parameters can be expressed as the posterior distribution

$$p(\mathbf{m}|\tilde{\mathbf{d}}) = \frac{p(\mathbf{m})p(\tilde{\mathbf{d}}|\mathbf{m})}{p(\tilde{\mathbf{d}})}, \tag{2}$$

where $p(\mathbf{m})$ is the prior distribution of $\mathbf{m}$, $p(\tilde{\mathbf{d}}|\mathbf{m})$ demotes the likelihood function, and $p(\tilde{\mathbf{d}}) = \int p(\tilde{\mathbf{d}}|\mathbf{m})p(\mathbf{m})d\mathbf{m}$ signifies the evidence, a normalization constant.

For complex problems, analytical form of $p(\mathbf{m}|\tilde{\mathbf{d}})$ is not available, and Monte Carlo methods can be employed to approximate the posterior. According to the background knowledge of $\mathbf{m}$, N_e random samples can be drawn to form the prior ensemble, $\mathbf{M}^0 = \{\mathbf{m}_i^0 | i = 1, \dots, N_\mathrm{e}\}$. With the numerical model, the corresponding model outputs can be calculated, i.e., $\mathbf{D}^0 = \{\mathbf{d}_i^0 =$

$\mathcal{F}(\mathbf{m}_i^0)|i = 1, \dots, N_\mathrm{e}\}$. Below we will introduce how to update $\mathbf{M}^0$ from $\tilde{\mathbf{d}}$ with various DA methods, including ESMDA, ILUES, ESDL and PEDL.

2.1 Ensemble Smoother with Multiple Data Assimilation: ESMDA

Using the Kalman formula, we can update each sample in $\mathbf{M}^0$ as follows:

$$\mathbf{m}_i^1 = \mathbf{m}_i^0 + \mathbf{C}_{\mathrm{MD}}^0(\mathbf{C}_{\mathrm{DD}}^0 + \mathbf{C}_\mathrm{D})^{-1}\left(\tilde{\mathbf{d}} + \boldsymbol{\varepsilon}_i - \mathbf{d}_i^0\right), \tag{3}$$

where $\mathbf{M}^1 = \{\mathbf{m}_i^1|i = 1, \dots, N_\mathrm{e}\}$ is the updated ensemble representing our posterior understanding about the model parameters, $\mathbf{C}_{\mathrm{MD}}^0$ is the cross-covariance between $\mathbf{M}^0$ and $\mathbf{D}^0$, $\mathbf{C}_{\mathrm{DD}}^0$ is the auto-covariance of $\mathbf{D}^0$, and $\boldsymbol{\varepsilon}_i$ is a random realization of measurement errors, respectively. For highly nonlinear problems, iterative application of the Kalman updating of equation (3) can be adopted:

$$\mathbf{m}_i^t = \mathbf{m}_i^{t-1} + \mathbf{C}_{\mathrm{MD}}^{t-1}(\mathbf{C}_{\mathrm{DD}}^{t-1} + \alpha^t\mathbf{C}_\mathrm{D})^{-1}\left(\tilde{\mathbf{d}} + \sqrt{\alpha^t}\boldsymbol{\varepsilon}_i - \mathbf{d}_i^{t-1}\right), \tag{4}$$

where $t = 1, \dots, N_{\mathrm{iter}}$, α^t is the inflation factor that satisfies $\sum_{t=1}^{N_{\mathrm{iter}}} 1/\alpha^t = 1$, and N_{iter} is the iteration number. Finally, we use $\mathbf{M}^{N_{\mathrm{iter}}} = \left\{\mathbf{m}_i^{N_{\mathrm{iter}}}|i = 1, \dots, N_\mathrm{e}\right\}$ to approximate the posterior distribution of $\mathbf{m}$. For the theory and implementation details of ESMDA, one can refer to (Emerick & Reynolds, 2013).

2.2 Iterative Local Updating Ensemble Smoother: ILUES

When the posterior distribution of parameters $\mathbf{m}$ exhibits multiple modes, signifying that distinct parameter sets can equally reproduce the measurement data, the straightforward application of ESMDA may lead to biased results. This phenomenon, known as the equifinality issue, is a common challenge encountered in DA for complex systems, particularly when the available information contained in the measurement data is insufficient. To reasonably represent the multi-modal posterior distribution, J Zhang et al. (2018) proposed to identify and update the local ensemble of each sample $\mathbf{m}_i^{t-1}$ in $\mathbf{M}^{t-1}$ independently at iteration $t = 1, \dots, N_{\mathrm{iter}}$. The local ensemble of $\mathbf{m}_i^{t-1}$ is based on the following measure:

$$\mathcal{J}(\mathbf{m}) = \mathcal{J}_1(\mathbf{m})/\mathcal{J}_1^{\max} + \mathcal{J}_2(\mathbf{m})/\mathcal{J}_2^{\max}, \tag{5}$$

where $\mathcal{J}_1(\mathbf{m}) = (\mathbf{m} - \mathbf{m}_i^{t-1})\mathbf{C}_{\mathrm{MM}}^{-1}(\mathbf{m} - \mathbf{m}_i^{t-1})^{\mathrm{T}}$, $\mathcal{J}_2(\mathbf{m}) = \left(\mathcal{F}(\mathbf{m}) - \tilde{\mathbf{d}}\right)\mathbf{C}_{\mathrm{D}}^{-1}\left(\mathcal{F}(\mathbf{m}) - \tilde{\mathbf{d}}\right)^{\mathrm{T}}$, $\mathbf{C}_{\mathrm{MM}}$ is the auto-covariance of model parameters, $\mathcal{J}_1^{\max}$ is the maximum value of $\mathcal{J}_1$, and $\mathcal{J}_2^{\max}$ is the maximum value of $\mathcal{J}_2$, respectively. The local ensemble of $\mathbf{m}_i^{t-1}$ is the $N_{\mathrm{L}} = \beta N_{\mathrm{e}}$ $(0 < \beta \leq 1)$ samples in $\mathbf{M}^{t-1}$ with the smallest $\mathcal{J}$ values, i.e., $\mathbf{M}_i^{t-1} = \left\{\mathbf{m}_{i,j}^{t-1} | j = 1, \dots, N_{\mathrm{L}}\right\}$. Each sample in $\mathbf{M}_i^{t-1}$ can be updated as:

$$\mathbf{m}_{i,j}^{t} = \mathbf{m}_{i,j}^{t-1} + \mathbf{C}_{i,\mathrm{MD}}^{t-1}\left(\mathbf{C}_{i,\mathrm{DD}}^{t-1} + \alpha^t \mathbf{C}_{\mathrm{D}}\right)^{-1}\left(\tilde{\mathbf{d}} + \sqrt{\alpha^t}\boldsymbol{\varepsilon}_j - \mathbf{d}_{i,j}^{t-1}\right), \tag{6}$$

where $\mathbf{C}_{i,\mathrm{MD}}^{t-1}$ is the cross-covariance between $\mathbf{M}_i^{t-1}$ and $\mathbf{D}_i^{t-1} = \left\{\mathbf{d}_{i,j}^{t-1} = \mathcal{F}\left(\mathbf{m}_{i,j}^{t-1}\right) | j = 1, \dots, N_{\mathrm{L}}\right\}$, $\mathbf{C}_{i,\mathrm{DD}}^{t-1}$ is the auto-covariance of $\mathbf{D}_i^{t-1}$, respectively. The updated sample of $\mathbf{m}_i^{t-1}$, i.e., $\mathbf{m}_i^t$, can be randomly drawn from the updated local ensemble, $\mathbf{M}_i^t = \left\{\mathbf{m}_{i,j}^t | j = 1, \dots, N_{\mathrm{L}}\right\}$. Finally, we use $\mathbf{M}^{N_{\mathrm{iter}}} = \left\{\mathbf{m}_i^{N_{\mathrm{iter}}} | i = 1, \dots, N_{\mathrm{e}}\right\}$ to approximate the posterior distribution of $\mathbf{m}$ with possible multi-modes. More details about ILUES can be found in (J Zhang et al., 2018).

2.3 Ensemble Smoother with Deep Learning-based Update: ESDL

Essentially, the Kalman update used in ESMDA and ILUES builds a linear relationship between the innovation vector, $\Delta\mathbf{d}_i^t = \tilde{\mathbf{d}} + \sqrt{\alpha^t}\boldsymbol{\varepsilon}_i - \mathbf{d}_i^{t-1}$, and the update vector, $\Delta\mathbf{m}_i^t = \mathbf{m}_i^t - \mathbf{m}_i^{t-1}$:

$$\Delta\mathbf{m}_i^t = \mathbf{K}^t \Delta\mathbf{d}_i^t, \tag{7}$$

where $\mathbf{K}^t = \mathbf{C}_{\mathrm{MD}}^{t-1}(\mathbf{C}_{\mathrm{DD}}^{t-1} + \alpha^t \mathbf{C}_{\mathrm{D}})^{-1}$ is the so-called Kalman gain matrix. As the above calculation is only based on the mean and covariance, the Kalman-based DA is subjected to the Gaussian assumption. Inspired by the universal approximation and pattern recognition abilities of DL, J Zhang et al. (2020) proposed to supplant the Kalman-based update in EnKF and its variants with a DL-based counterpart:

$$\Delta\mathbf{m}_i^t = \mathcal{G}_{\mathrm{DL}}^t(\Delta\mathbf{d}_i^t), \tag{8}$$

where $\mathcal{G}_{\mathrm{DL}}^t(\cdot)$ is a nonlinear mapping from the innovation vector to the update vector based on DL. The effective training of $\mathcal{G}_{\mathrm{DL}}^t(\cdot)$ can be facilitated by the vast amount of data directly generated from $\mathbf{M}^{t-1}$ and $\mathbf{D}^{t-1}$, i.e., $\mathbf{X}^t = \left\{\mathbf{x}_{\mathrm{input}} = \mathbf{d}_i^{t-1} + \sqrt{\alpha^t}\boldsymbol{\varepsilon}_{ij} - \mathbf{d}_j^{t-1}, \mathbf{x}_{\mathrm{target}} = \mathbf{m}_i^{t-1} - \mathbf{m}_j^{t-1} | i = 1, \dots, N_{\mathrm{e}} - 1, i < j \leq N_{\mathrm{e}}\right\}$. Here, we treat $\{\mathbf{m}_i^{t-1}, \mathbf{d}_i^{t-1}\}$ as the synthetic truth and can

produce $N_e - 1$ pairs of innovation and update vectors from the rest ensemble members. In total, there are $C_{N_e}^2 = N_e(N_e - 1)/2$ training samples in $\mathbf{X}^t$. Results shown that ESDL can better solve DA problems involving high-dimensional and non-Gaussian distributed parameters than its Kalman-based counterpart (J Zhang et al., 2020).

2.4 Parameter Estimator with Deep Learning: PEDL

In ESDL, what $\mathcal{G}_{\mathrm{DL}}^t(\cdot)$ tries to capture is the relationship between the increment in parameters, i.e., $\Delta\mathbf{m}_i^t$, and the displacement in model responses, i.e., $\Delta\mathbf{d}_i^t$, and the updated parameters are obtained as:

$$\mathbf{m}_i^t = \mathbf{m}_i^{t-1} + \Delta\mathbf{m}_i^t. \tag{9}$$

In the context of fractured media, $\mathbf{m}$ describe the spatial distribution of hydraulic properties, encompassing distinct parameter values (high values for the fractures, and low values for the matrix). During the training of $\mathcal{G}_{\mathrm{DL}}^t(\cdot)$, the information about the starting point of $\Delta\mathbf{m}_i^t$, i.e., $\mathbf{m}_i^{t-1}$, is not considered. Consequently, there is a potential mismatch between the regions with high and low values in $\mathbf{m}_i^{t-1}$ and $\Delta\mathbf{m}_i^t$, as the inferences made by $\mathcal{G}_{\mathrm{DL}}^t(\cdot)$ are not flawless. When $\mathbf{m}_i^{t-1}$ and $\Delta\mathbf{m}_i^t$ are added up, this imperfection can lead to irregularities in the fracture networks inferred by ESDL, as illustrated in Figure 5 (Section 3.1.2), highlighting this limitation.

To tackle this concern, here we modify ESDL by shifting the target of DL from the update vector $\Delta\mathbf{m}_i^t$ to the target parameter set $\mathbf{m}_i^t$ directly:

$$\mathbf{m}_i^t = \mathcal{G}_{\mathrm{DL}}^t\left(\mathbf{m}_i^{t-1}, \tilde{\mathbf{d}} + \sqrt{\alpha^t}\boldsymbol{\varepsilon}_i, \mathbf{d}_i^{t-1}\right). \tag{10}$$

To distinguish it from ESDL, we have named the new method PEDL (parameter estimator with DL). PEDL avoids the use of the difference vectors in ESMDA, ILUES and ESDL. Thus, the mismatches between $\mathbf{m}_i^{t-1}$ and $\Delta\mathbf{m}_i^t$ in ESDL will not affect the results anymore. However, the implementation of PEDL as described in equation (10) is ambiguous. After comprehensive testing, we suggest to adopt a simplified form of equation (10), i.e.,

$$\mathbf{m}_i^t = \mathcal{G}_{\mathrm{DL}}^t\left(\tilde{\mathbf{d}} + \sqrt{\alpha^t}\boldsymbol{\varepsilon}_i\right). \tag{11}$$

Here, the training data for the DL model are $\{\mathbf{x}_{\text{input}} = \mathbf{d}_i^{t-1} + \sqrt{\alpha^t}\boldsymbol{\varepsilon}_i, \mathbf{x}_{\text{target}} = \mathbf{m}_i^{t-1} | i = 1, \dots, N_{\text{e}}\}$. As will be demonstrated in latter part of this work, this new method is very easy to implement, and can obtain more reliable estimations of fractured media than the other three DA methods, i.e., ESMDA, ILUES, and ESDL.

3 Illustrative Case Studies

3.1 Case 1: Data Assimilation without Considering Model Structural Error

3.1.1 Model Settings

In this section, we set up a case study involving transient groundwater flow in a two-dimensional (2-D) fractured aquifer to evaluate the performance of PEDL. We employ the SC model (Tsang et al., 1996) as both the reference model providing the ground truth and the forecast model used in DA. In this context, we can disregard the error stemming from model structures, allowing us to directly compare the performance of PEDL with ESMDA, ILUES, and ESDL.

The flow domain is 205[L]×205[L] (in unit of length) and is discretized into 41×41 grids with a uniform spacing of 5[L] in the numerical model. All four lateral boundaries are impermeable. The domain predominantly consists of a matrix with permeability of $k_{\text{m}} = 10^{-13}[\text{L}^2]$, but there exist regions with considerably higher permeability values due to the presence of fractures. Figure 1 illustrates the reference distribution of the fractured zones, with isotropic permeability of $k_{\text{f}} = 90k_{\text{m}}$. The simulation period spans $T_{\text{s}} = 86400\,[\text{T}]$ (in unit of time) and is evenly divided into 20 timesteps. The initial pressure across the entire domain is $p_0 = 10^7[\text{ML}^{-1}\text{T}^{-2}]$, where [M] represents any consistent unit of mass. An injection well (I) at the center of the domain conducts water injection at a constant rate of $Q_0 = 0.1[\text{L}^2\text{T}^{-1}]$, and eight pumping wells (P1-P8) initiate pumping at a constant pressure of $0.5p_0$. The pressure dynamics are described by the following equation:

$$\phi c_{\text{rw}} \frac{\partial p}{\partial t} = \nabla \cdot \left(\frac{\mathbf{k}}{\mu} \nabla p\right) + q, \tag{12}$$

where ϕ is the porosity of medium (-), c_{rw} is the total compressibility of rock and water $[\text{M}^{-1}\text{LT}^2]$, p is the hydraulic pressure $[\text{ML}^{-1}\text{T}^{-2}]$, t is the time [T], $\mathbf{k}$ is the permeability tensor $[\text{L}^2]$, μ is the water viscosity $[\text{ML}^{-1}\text{T}^{-1}]$, and q is the source/sink term $[\text{T}^{-1}]$, respectively. Here,

$\phi = 0.3$, $c_{\mathrm{rw}} = 6 \times 10^{-10}[\mathrm{M^{-1}LT^2}]$, and $\mu = 10^{-3}[\mathrm{ML^{-1}T^{-1}}]$. In this scenario, the tensor $\mathbf{k}$ are simplified into a location-dependent scalar function, $k(x, y)$, where the values within the 1681 cells constitute the sole unknown parameters that need calibration. The governing equation is numerically solved with the MATLAB Reservoir Simulation Toolbox (Lie & Møyner, 2021).

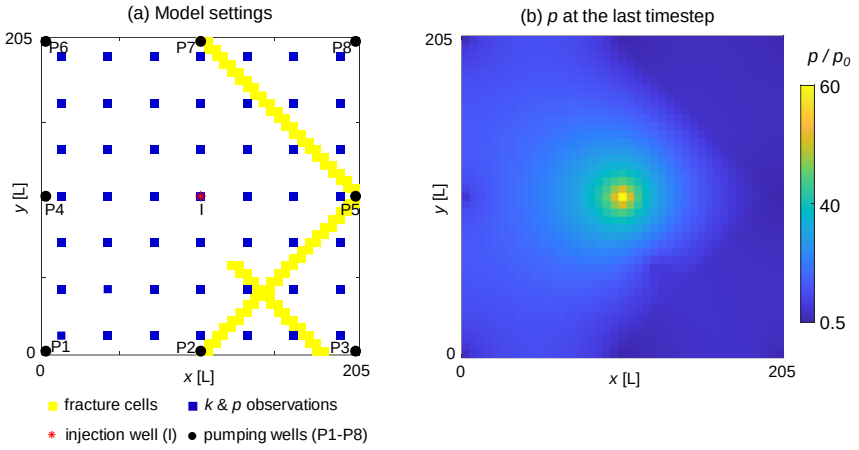

Figure 1. (a) Schematic overview of the model settings in Case 1. All four boundaries are impermeable. An injection well is positioned at the domain's center, and eight pumping wells (P1-P8) are situated near the boundaries. The blue cells indicate locations where measurements of k and p are acquired. The yellow cells depict the reference distribution of fractures. (b) Distribution of pressure (p) at the last timestep, highlighting the influence of fractured cells.

The observational dataset employed for inferring the distribution of $k(x, y)$ includes 49 permeability (k) values at the blue nodes (as shown in Figure 1a), 49 pressure (p) values at the same nodes at 21 timesteps (49×21 values in total), and 9 flowrates (Q) values at the single injection well and eight pumping wells at the 21 timesteps (9×21 values in total). The observation errors associated with k, p, and Q are modeled with Gaussian distributions, i.e., $\varepsilon_k \sim \mathcal{N}(0, \sigma_k^2)$, $\varepsilon_p \sim \mathcal{N}(0, \sigma_p^2)$, and $\varepsilon_Q \sim \mathcal{N}(0, \sigma_Q^2)$, where $\sigma_k = 5k_{\mathrm{m}}$, $\sigma_p = 0.05p_0$, and $\sigma_Q = 0.005Q_0$, respectively. In the reference model, there are 106 fractured cells, comprising approximately 6.3% of the total cells. These high-permeability fracture zones are indicated by the yellow cells in Figure 1(a). Figure 1(b) illustrates the pressure distribution in the reference model at the last timestep, clearly demonstrating the impact of these high-permeability fractured zones.

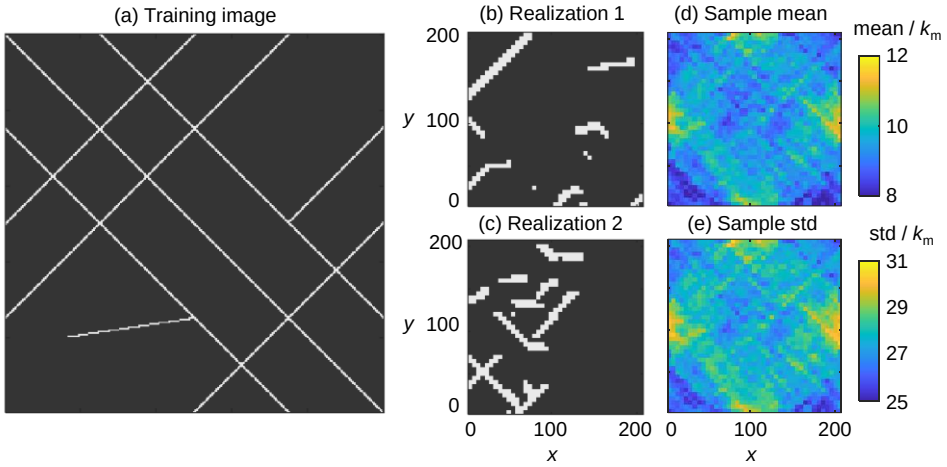

Figure 2. (a) The training image used to generate random realizations of the k field; (b-c) two realizations of the k field, and (d-e) the mean and standard deviation (std) of the k field.

The direct sampling method, as described by Mariethoz et al. (2010), is utilized to generate random realizations of the $k(x, y)$ field, each field having a dimension of $N_{\mathrm{k}} = 41 \times 41$. These realizations are generated based on a training image that includes background information about fractures, such as potential orientation and density (as shown in Figure 2a). In the generated k realizations, black cells are designated as k_{m}, representing the matrix category, while white cells are designated as k_{f}, signifying the fracture category. In Figures 2(b-c), we present two random samples of the generated k fields. The sample mean and standard deviation (std) fields calculated from all the realizations are depicted in Figures 2(d-e).

3.1.2 Results from Four DA Methods

Four DA methods, namely ESMDA, ILUES, ESDL, and PEDL, are applied to estimate the k field across the flow domain. All methods, except for PEDL (without iteration, $N_{\mathrm{e}} = 5000$), undergo five iterations with an ensemble size of $N_{\mathrm{e}} = 5000$. In the case of ILUES, the hyper-parameter β, which dictates the selection of the local ensemble, is set to 0.1. For both ESDL and PEDL, we have adopted the U-net architecture initially proposed by Ronneberger et al. (2015), as depicted in Figure 7(a). Given the presence of three distinct types of measurement data—permeability (k), flowrate (Q), and pressure (p)—each with varying dimensionalities, we employ three U-net blocks to process each data type. Subsequently, we concatenate and further process these data streams until the target (the 41×41 k field) is reached. In both ESDL and PEDL, the

DL model is trained using the Adam optimizer with a consistent learning rate of 0.001. The training process consists of 100 epochs, with a batch size of 256.

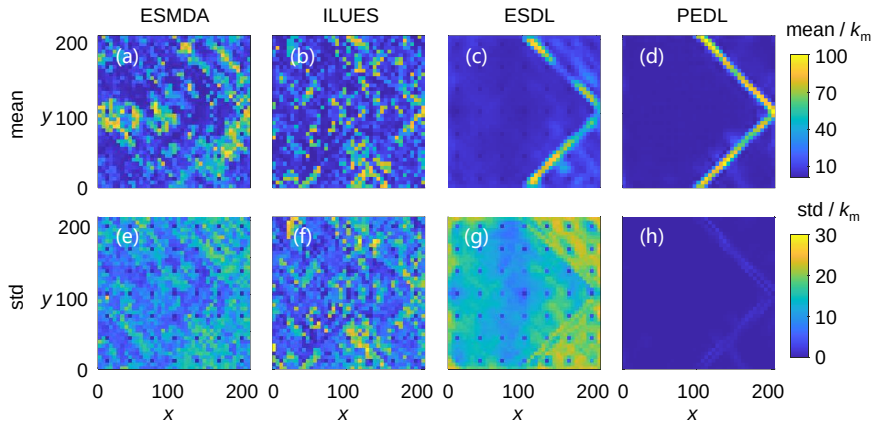

Figure 3. (a-d) Mean and (e-h) standard deviation (std) of the estimated k fields obtained by ESMDA, ILUES, ESDL, and PEDL, respectively. Note that all the means and stds are expressed as multiples of k_{m}.

The normalized root-mean-square errors (NRMSEs) relative to the matrix permeability k_{m}, between the estimated mean ($\bar{k}$) and the reference (k^*) fields, i.e.,

$$\mathrm{NRMSE} = \frac{1}{k_{\mathrm{m}}}\sqrt{\frac{1}{N_{\mathrm{k}}}\sum_{i=1}^{N_{\mathrm{k}}}\left(\bar{k}_i - k_i^*\right)^2}, \tag{13}$$

are obtained as follows: ESMDA (32.31), ILUES (30.03), ESDL (15.89), and PEDL (12.11). It is worth noting that the NRMSE value between the initial mean k field and the reference k field is 22.35. The NRMSE values for ESMDA and ILUES exceed that of the initial mean field, indicating the occurrence of filter divergence in these two methods. With the DL-based update, ESDL can obtain improved estimation of k, but the reduction in NRMSE from the initial field is not very large. Without requiring iterations, PEDL can obtain the best match of the highly complex parameter field.

Figure 3 illustrates the mean and standard deviation (std) of the k fields estimated by these four DA methods. It is evident that PEDL effectively captures the distribution of fracture cells (highly permeable zones) with low uncertainty, albeit with some minor details missing. Conversely,

neither ESMDA nor ILUES provide a satisfactory estimation of k. On the other hand, ESDL partially recognizes the fracture structure. Specifically, ESDL tends to overestimate the k values in non-fractured areas near the upper-right and lower-right corners, and the standard deviation of the k field obtained by ESDL is significantly higher than those obtained using other methods.

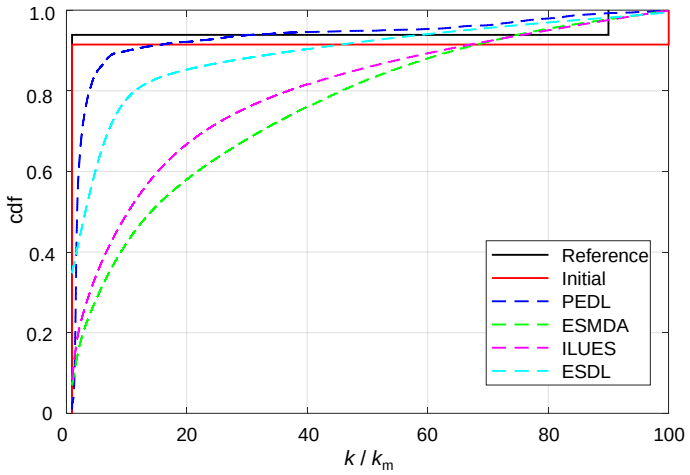

Figure 4. Cumulative distribution functions (cdfs) for the reference k field, initial k realizations, and estimated k fields from PEDL, ESMDA, ILUES, and ESDL, respectively.

Given the strong non-Gaussian nature of this problem, it is necessary to consider more information beyond the mean and standard deviation to thoroughly evaluate the results. Figure 4 displays the cumulative distribution functions (cdfs) of the updated k fields for all four methods, as well as the reference and initial k fields. It is evident that PEDL produces a cdf of k field that closely resembles the stepwise cdf of the reference k field, demonstrating PEDL's ability to handle strong non-Gaussianity.

Moreover, to monitor the evolution of individual k field samples before and after the various updates, we compare four randomly selected realizations in Figure 5. It reveals that initially distinct realizations (the first row of Figure 5) tend to converge and approach the reference k field after the update with PEDL (the last row of Figure 5). This consistency aligns with the observed low k standard deviation values across the entire domain (as seen in Figure 3h). Conversely, the first three rows of Figure 5 demonstrate that in both ESMDA and ILUES, the updated realizations do exhibit some degree of convergence among them, but they do not resemble the reference k field. This suggests the occurrence of filter divergence. In the case of

ESDL (the fourth row), while high-permeability stripes akin to the reference field do emerge in the updated k realizations, the initial random structures of fracture in the four realizations largely persist, resulting in substantial irregularities within the final realizations. One possible explanation for this behavior is that the $\{\Delta\mathbf{m}^t, \Delta\mathbf{d}^t\}$ pairs may vary significantly for different $\{\mathbf{m}^{t-1}, \mathbf{d}^{t-1}\}$ in nonlinear problems, yet they are not considered during the model training process. The high values in $\mathbf{m}^{t-1}$ only partially cancel out the values at the same locations in $\Delta\mathbf{m}^t$, causing the unwanted irregularities in each realization. Although these irregularities can be averaged out in the ensemble mean, as shown in Figure 3(c), the large uncertainty do exist in the standard deviation field (Figure 3g).

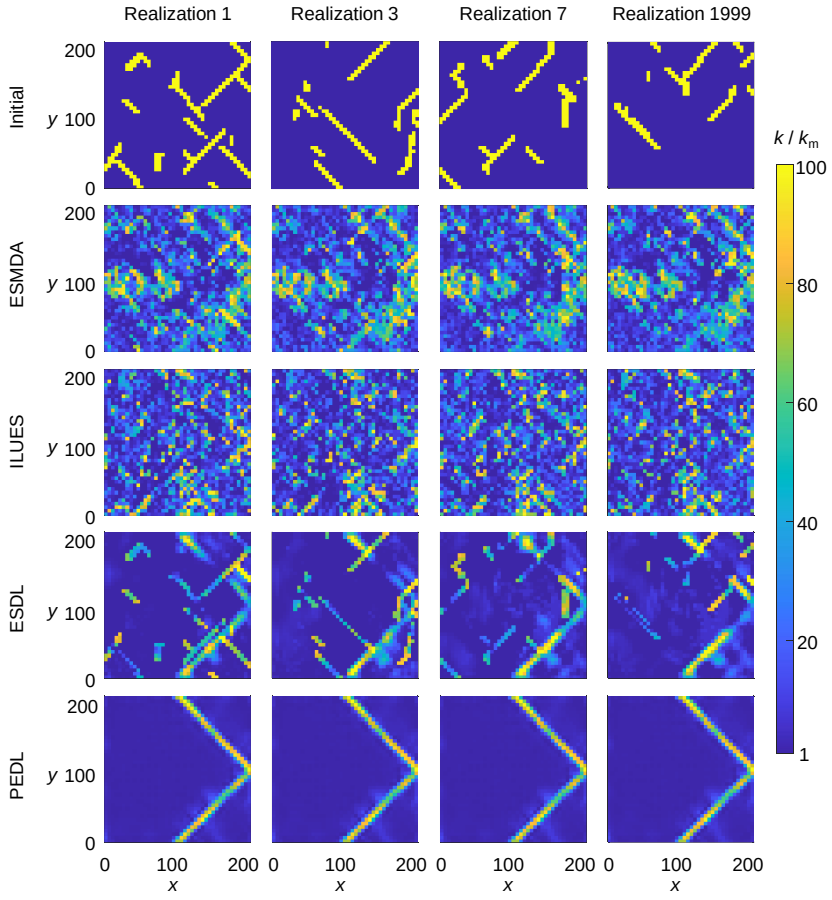

Figure 5. Four randomly sampled initial k fields and the corresponding updated ones with ESMDA, ILUES, ESDL, and PEDL, respectively. All k fields are expressed as multiples of k_{m}.

From the results above, it is concluded that while ESMDA, ILUES and ESDL encounter significant difficulties in this problem, PEDL yields much better estimation results from the perspective of ensemble behavior and individual realization performance.

3.1.3 Impact of Ensemble Size and Network Architecture

To assess the influence of ensemble size on PEDL's performance, we further conduct experiments using ensembles with various sizes ($N_e = 10^2$ to 10^5, as depicted in Figure 6). To ensure the statistical reliability of the results, we carried out twenty parallel tests for each ensemble size. Notably, Figure 6 highlights that the NRMSE values begin to decline when N_e exceeds 500 and stabilize as N_e surpasses 5,000. This observation is intriguing, as deep neural networks (DNNs) are typically associated with a demand for an extensive volume of training data.

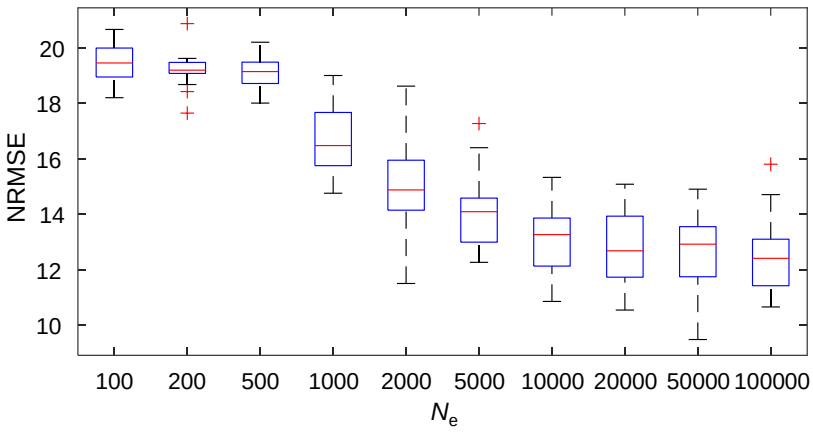

Figure 6. NRMSEs of results obtained by PEDL with various ensemble sizes.

In our prior experiment, PEDL utilized a U-net architecture for DL. However, it's natural to question whether alternative types of adequate DNNs can deliver comparable results within the PEDL framework. To investigate the impact of network architecture, we decide to substitute the U-net with a residual neural network (ResNet, shown in Figure 7b), while maintaining the ensemble size of $N_e = 5000$. The training settings for the ResNet model remain identical to those applied to U-net. Remarkably, the resulting NRMSE in this instance is 12.66, a value that closely aligns with the NRMSE of 12.11 achieved by PEDL with U-net.

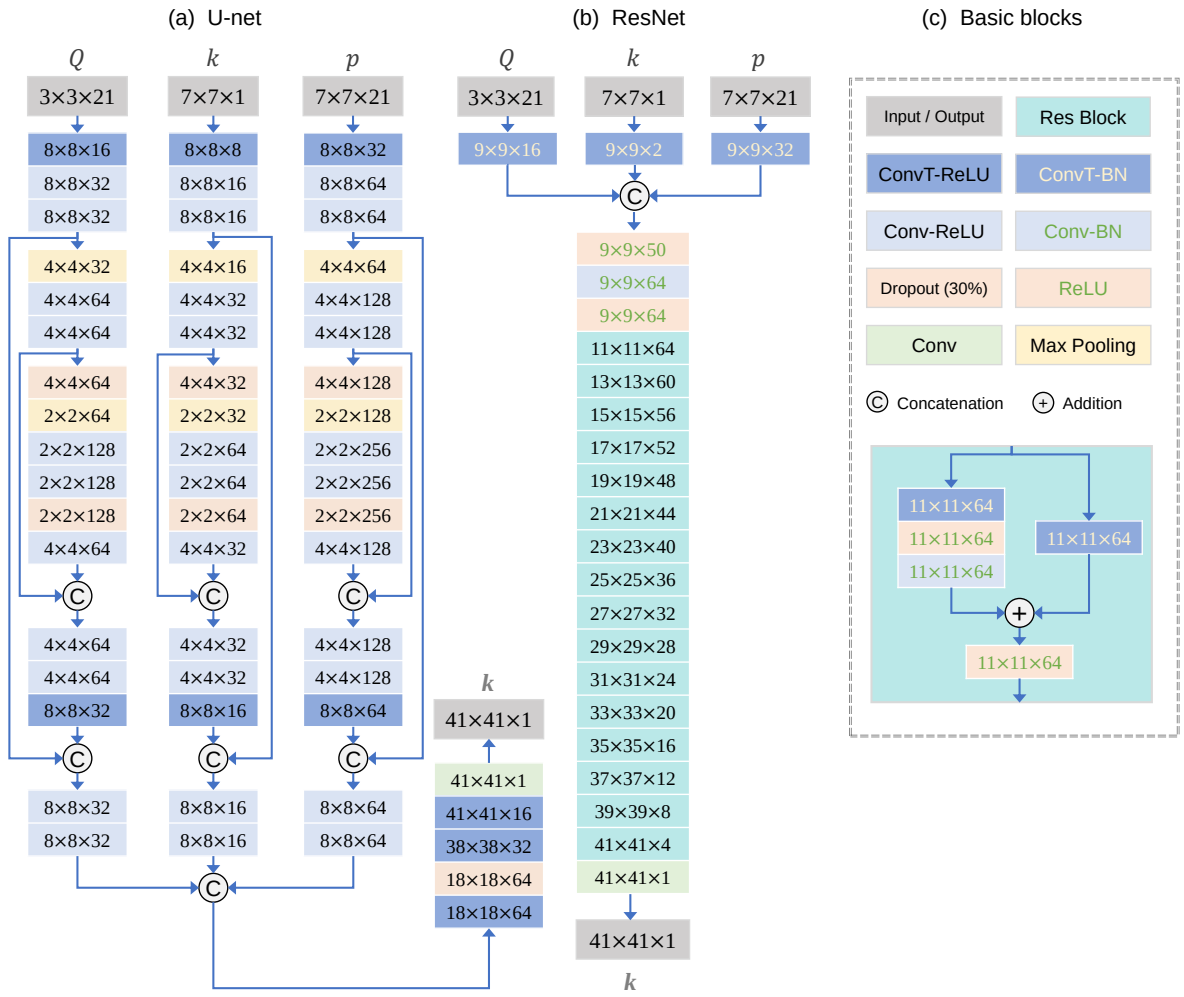

Figure 7. DL model architectures used in this study: (a) U-net, (b) ResNet, and (c) basic blocks used in U-net and ResNet, respectively. Here, Q, p, k represent flowrate, pressure, and permeability, as input or output, respectively. Conv and ConvT mean the 2-D convolution and the transposed 2-D convolution layers, ReLU denotes the rectified linear unit, and BN signifies the batch normalization layer, respectively.

In Figure 8, we present the spatial distributions of the mean and standard deviation of k fields obtained through the ResNet-based PEDL, along with four random realizations of updated k field. The results closely resemble the PEDL approach applied with the U-net (as seen in Figures 3 and 5). This observation underscores the fact that PEDL demonstrates satisfactory performance with both U-net and ResNet architectures. It is likely that using a better designed DL model can produce enhanced estimation of fractured media properties. Yet, the searching for the optimal DL model and training options are beyond the scope of the current work.

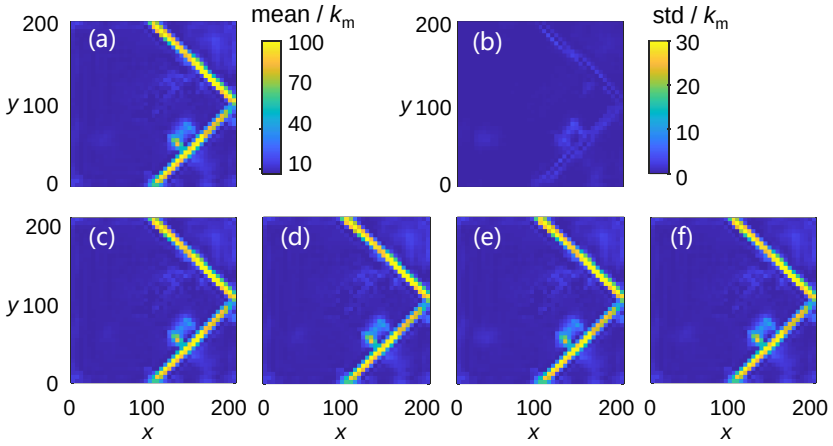

Figure 8. Results obtained by PEDL using ResNet: (a) mean of the updated k fields, (b) standard deviation of the updated k fields, and (c-f) four random realizations of the updated k fields.

3.2 Case 2: Data Assimilation Considering Model Structural Error

In the previous section, the model structural error is not considered, and both the reference model and forecast model are based on the SC model. However, fractured media in the natural world often showcase significantly more pronounced complex and non-Gaussian behaviors than what can be accurately represented by the simplistic SC model. In this section, we shift our focus to the more accurate EDFM model, which serves as the reference model, to thoroughly assess the effectiveness of PEDL in addressing more complex scenarios. It's worth noting that when estimating the properties of the media through DA, we still employ the SC model, albeit introducing some degree of structural error into the model. In this section, we will subject PEDL to further testing within the context of model structural error to evaluate its robustness.

As the name implies, the EDFM model incorporates discrete fractures into the matrix as lower-dimensional entities, such as fracture lines within a 2-D matrix or fracture planes within a 3-D matrix. The EDFM model describes the flow within the matrix as follows:

$$\frac{\partial(\phi\rho)}{\partial t} = \nabla \cdot \left(\frac{\mathbf{k}}{\mu} \nabla(p - \rho g z) \right) + q^{(\mathrm{m})} - \sum_j q_j^{(\mathrm{mf})}, \tag{14}$$

where ρ means the density of water, g is the gravitational constant, z signifies the depth, $q^{(\mathrm{m})}$ denotes the source/sink term in the matrix cell, and $q_j^{(\mathrm{mf})}$ represents the exchange term from the matrix cell to the j-th fracture (set as zero if matrix cell and fracture are nonadjacent), respectively. The flow equation in the j-th fracture can be expressed as:

$$\frac{\partial\left(\phi_j^{(\mathrm{f})}\rho\right)}{\partial t} = \nabla\cdot\left(\frac{\mathbf{k}_j}{\mu}\nabla\left(p_j^{(\mathrm{f})} - \rho g z\right)\right) + \frac{1}{a_j}\left(q^{(\mathrm{f})} - q_j^{(\mathrm{fm})} - \sum_{i\neq j} q_{j,i}^{(\mathrm{ff})}\right), \tag{15}$$

where $\phi_j^{(\mathrm{f})}$ and $\mathbf{k}_j$ are the porosity and permeability of the j-th fracture, $p_j^{(\mathrm{f})}$ is the hydraulic pressure in the current cell of the j-th fracture, $q^{(\mathrm{f})}$ is the source/sink term in the fracture cell, $q_j^{(\mathrm{fm})}$ is the exchange from the j-th fracture to the surrounding matrix cell, $q_{j,i}^{(\mathrm{ff})}$ is the exchange from the j-th fracture to other fractures (set as zero if they don't intersect in the current cell), and a_j is the aperture of the j-th fracture, respectively.

The matrix-fracture exchanges $q_j^{(\mathrm{mf})}$ and $q_j^{(\mathrm{fm})}$, when calculated on cells, can be expressed as:

$$Q_j^{(\mathrm{mf})} = \int_{V_\mathrm{m}} q_j^{(\mathrm{mf})} dV = T^{(\mathrm{mf})}\left(p - p_j^{(\mathrm{f})}\right), \tag{16}$$

and

$$Q_j^{(\mathrm{fm})} = \int_{A_\mathrm{m}} q_j^{(\mathrm{fm})} dA = T^{(\mathrm{mf})}\left(p_j^{(\mathrm{f})} - p\right) = -Q_j^{(\mathrm{mf})}, \tag{17}$$

respectively. In the above equations, $T^{(\mathrm{mf})} = \frac{k^{(\mathrm{mf})}A^{(\mathrm{mf})}}{d^{(\mathrm{mf})}}$ is the transmissivity between matrix and fracture, $k^{(\mathrm{mf})}$ is the volume-weighted harmonic mean of fracture and matrix permeability, $A^{(\mathrm{mf})}$ is the exchange area between matrix and fracture cells, and $d^{(\mathrm{mf})}$ is the characteristic distance between matrix cell and fracture plane, respectively. The matrix-fracture exchanges calculated with equations (15-17) are sometimes called "non-neighboring connections" since the matrix and fracture cells are not neighbors in griding but connected by extra relations. For more details about the EDFM model, interested readers can refer to (Lie & Møyner, 2021; Moinfar et al., 2014).

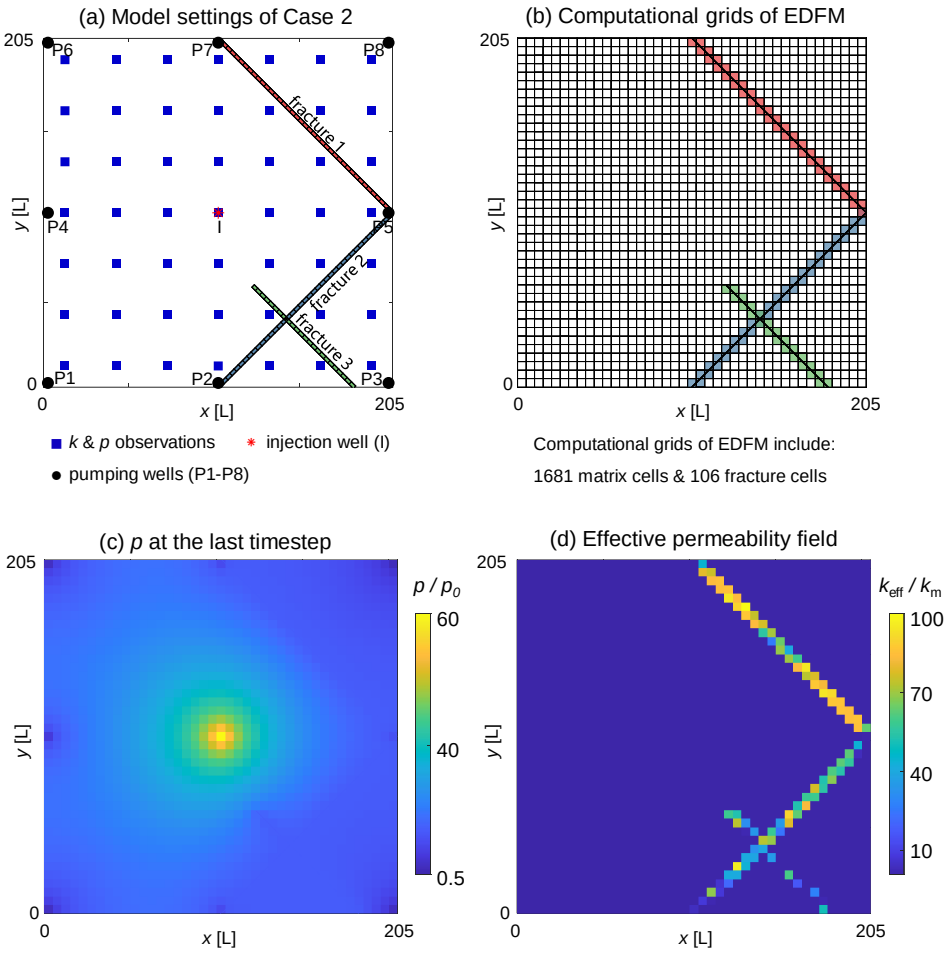

Figure 9. (a) Model settings of Case 2; (b) Computational grids of the EDFM model (colored cells are linked to fracture cells appended through non-neighboring connections); (c) Spatial distribution of pressure calculated with the EDFM model at the last timestep; (d) Effective permeability field found by an optimization method based on p and Q at all timesteps in the EDFM model.

In Case 2, we examine a fractured aquifer similar to the one in Case 1 (depicted in Figure 1), with the exception of the fracture part. In this aquifer, there are no high-permeability matrix cells. Instead, there are three fractures with permeability of $k_{\mathrm{f}}^{*} = 100k_{\mathrm{m}}$, porosity of $\phi = 0.8$, and aperture of $a = 0.2$[L] (as illustrated in Figure 9a). As in Case 1, the simulation period is set to be T_{s} =86400 [T], evenly divided into 20 timesteps. At $t = 0$[T], the pressure is uniformly set as $p_0 = 107[\mathrm{ML^{-1}T^{-2}}]$ across the domain. The injection and pumping wells are managed in the same manner as Case 1, i.e., one injection well located at the center of the domain with the rate of $0.1[\mathrm{L^2T^{-1}}]$, and eight pumping wells (P1-P8) extracting water at a fixed pressure of $0.5p_0$. As

shown in Figure 9(b), the matrix is discretized into 41×41 uniform grids, which divides the fractures into 106 fracture cells. In total, there are 109 identified non-neighboring connections, including three fracture-fracture connections. The pressure distribution calculated with the EDFM model at the last timestep is displayed in Figure 9(c). In this case, the EDFM model, acting as the reference model, is used to generate measurement data.

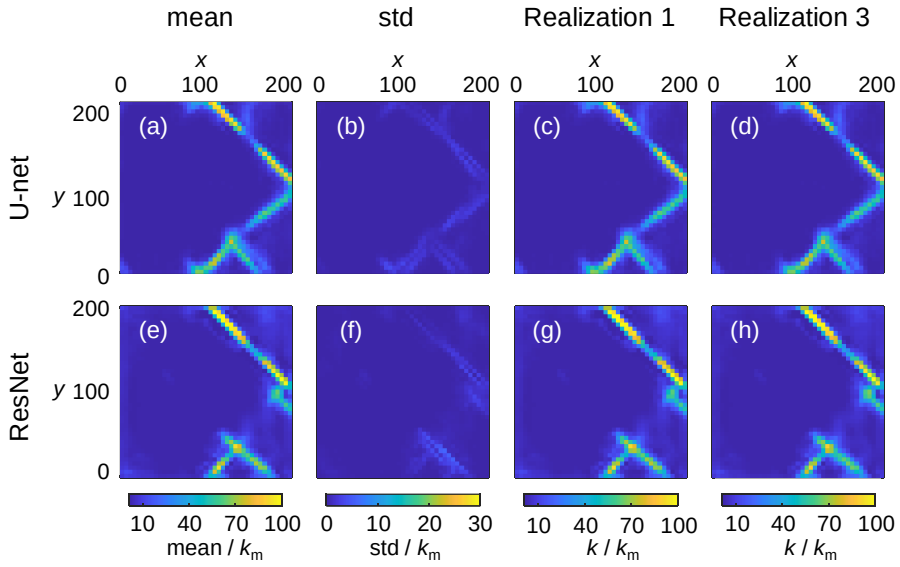

Figure 10. Results of permeability estimation in Case 2 using U-net-based PEDL (top row) and ResNet-based PEDL (bottom row), respectively. The mean estimates for the two methods are presented in subfigures (a) and (e), the estimation uncertainty measured by the standard deviation (std) are given in (b) and (f), and some random realizations are depicted in (c-d) and (g-h), respectively.

In the implementation of DA, the simpler SC model with 41×41 grids is adopted to calculate the model responses, due to its ease of implementation and prevalence in fractured aquifer characterization practices (National Academies of Sciences, 2020). Unlike the EDFM model, the SC model has no fracture cells or non-neighboring connections. The impact of actual fractures is reflected in the effective permeability field (EPF) of matrix. To evaluate the performance of PEDL, a "pseudo-reference" of EPF for the SC model is found by solving a nonlinear data fitting problem with the trust-region-reflective algorithm (Coleman & Li, 1996) based on the complete data of p and Q at all grids and timesteps from the EDFM model simulation. At each timestep, there are 1681 p values and nine Q values. The obtained EPF is shown in Figure 10(d), which is used to calculate the NRMSE values of the updated k fields obtained by PEDL.

The measurement data from the same observation network (Figure 9a) as in Case 1 are used in the estimation of k field here, i.e., 49 k values and 49×21 p values at the 7×7 blue nodes, and 9×21 Q values at the single injection well and eight pumping wells. Figure 10 shows the estimated mean, std and two arbitrarily picked realizations of k field by U-net-based PEDL (top row) and ResNet-based PEDL (bottom row). Evidently, PEDL demonstrates the capacity to capture the fundamental structure of fractures, employing either the U-net or ResNet architecture. Notably, there are no remarkable distinctions between the mean estimate and individual realizations, underscoring the consistency of PEDL's performance. Additionally, PEDL exhibits NRMSE values of 16.02 for U-net and 15.07 for ResNet. While these NRMSEs may not reach the levels observed in Case 1 (with NRMSE values close to 12), they remain quite acceptable, given the presence of model structural error introduced by adopting the simplified SC model in DA.

4 Conclusions and Discussions

Water flow and solute transport in fractured media exhibit distinct characteristics, characterized by the notable non-Gaussian distribution of media properties and the substantial non-linearity in the underlying processes. Accurately estimating the heterogeneous hydraulic parameters of fractured media is of utmost importance for reliable predictions and well-informed decision-making. Nevertheless, the complexities arising from the high dimensionality and non-Gaussian nature of fractured media present substantial challenges for traditional DA methods, such as MCMC and EnKF, when aiming to achieve a robust estimation of these intricate properties. Previous attempts to facilitate the effective application of these DA methods have primarily relied on reparameterization techniques, involving the transformation of non-Gaussian variables into Gaussian ones. However, the use of these techniques can result in the loss of essential information related to the true nature of fractured media.

DL, known for its proficiency in modeling complex, nonlinear relationships and identifying intricate patterns within data, can improve DA by addressing the challenges arising from high-dimensionality and non-Gaussianity concurrently. J Zhang et al. (2020) proposed the innovative use of DL to create a nonlinear updating scheme, replacing the traditional linear Kalman formulation widely employed across various research domains. This DA method, named ESDL,

offers a superior capacity to capture the non-Gaussian characteristics of subsurface media's parameter fields compared to its Kalman-based counterparts. In our study, we applied ESDL for the first time to estimate hydraulic parameter fields within fractured media, comparing it with two Kalman-based DA methods, ESMDA(Emerick & Reynolds, 2013) and ILUES (J Zhang et al., 2018). Our findings demonstrate that ESDL significantly enhances the characterization of fractured media over ESMDA and ILUES. However, we observed some irregularities in the fracture networks inferred by ESDL, potentially attributable to the transition process from the innovation vector (the difference between observations and model predictions) to the update vector (the difference between posterior and prior parameters). Based on this insight, we enhanced ESDL by introducing a new updating scheme. The resulting DA method, named parameter estimator with DL (PEDL), establishes a direct update from the multi-source observation vector to the posterior parameter vector. PEDL surpasses ESDL in the same fracture characterization problem. In our sensitivity analysis regarding ensemble size, we observed that PEDL improves permeability estimates when utilizing ensemble sizes up to 5000. This is noteworthy, as DL models typically require a substantial volume of training data. Thus, an ensemble size not exceeding 10,000 appears as a reasonable compromise between inference accuracy and computational efficiency. Furthermore, PEDL's adaptability is evident in its flexibility regarding the architecture of the DL model employed. We verified this by testing two distinct model architectures, U-net and ResNet, within the PEDL framework, both of which yield similar estimation results in two case studies with increasing complexity. Additionally, we evaluated PEDL's performance in the presence of structural model error. Specifically, we used the sophisticated EDFM model as the reference model to generate measurement data but adopted the simplified SC model as the forecast model in DA. In this scenario, the ground truth exhibited heightened non-Gaussian and nonlinear characteristics, mirroring the complexities typically encountered in practical applications. Although PEDL, utilizing either U-net or ResNet, could not achieve an exact match between the forecast model and the ground truth, it displayed the ability to discern the fundamental structure of actual fractures, albeit with slightly reduced performance in comparison to Case 1, due to the presence of model structural error.

In the current study, we investigate two cases featuring only three fractures. While our tests have unequivocally demonstrated the effectiveness of PEDL, it is imperative to address more intricate scenarios in future research endeavors. The presence of more fractures introduces formidable

challenges to both modeling and DA techniques. To construct an adequate numerical model, it is essential to enhance the discretization in both spatial and temporal domains. Naturally, this will lead to a substantial increase in simulation time. To bolster simulation efficiency, one can consider adopting surrogate models or low-fidelity approximations. Striking a balance between efficiency and accuracy, a promising solution may involve leveraging multi-fidelity simulations underpinned by DL techniques, as suggested by Chakraborty (2021). Furthermore, to comprehensively characterize more complex geological media, we must expand our data collection efforts to improve information content. This entails considering various types of measurements, including electromagnetic and electrical resistivity tomography data. The intricate nature of the models and the data necessitates the development of a more sophisticated DL model and an updated formula for PEDL.

Open Research

The data and codes on which this article is based are available in (Nan & Zhang, 2023).

Acknowledgments

This study is supported by the Fundamental Research Funds for the Central Universities (B220201023 and B210201011), Jiangsu Provincial Innovation and Entrepreneurship Doctor Program (Grant JSSCBS20210260), and National Natural Science Foundation of China (41972245 and 42277190).

References

Abarbanel, H. D. I., Rozdeba, P. J., & Shirman, S. (2018). Machine Learning: Deepest Learning as Statistical Data Assimilation Problems. *Neural Computation*, *30*(8), 2025-2055. https://doi.org/10.1162/neco_a_01094

Berre, I., Doster, F., & Keilegavlen, E. (2019). Flow in fractured porous media: A review of conceptual models and discretization approaches. *Transport in Porous Media*, *130*(1), 215-236. https://doi.org/10.1007/s11242-018-1171-6

Berry, T., & Harlim, J. (2017). Correcting Biased Observation Model Error in Data Assimilation. *Monthly Weather Review*, *145*(7), 2833-2853. https://doi.org/10.1175/mwr-d-16-0428.1

Beven, K., & Freer, J. (2001). Equifinality, data assimilation, and uncertainty estimation in mechanistic modelling of complex environmental systems using the GLUE methodology. *Journal of Hydrology*, *249*(1-4), 11-29. https://doi.org/10.1016/S0022-1694(01)00421-8

503 Blaheta, R., Béreš, M., Domesová, S., & Horák, D. (2020). Bayesian inversion for steady flow in fractured porous
504 media with contact on fractures and hydro-mechanical coupling. *Computational Geosciences*, *24*, 1911-1932.
505 https://doi.org/10.1007/s10596-020-09935-8

506 Cacas, M.-C., Ledoux, E., de Marsily, G., Tillie, B., Barbreau, A., Durand, E., Feuga, B., & Peaudecerf, P. (1990).
507 Modeling fracture flow with a stochastic discrete fracture network: calibration and validation: 1. The flow model.
508 *Water Resources Research*, *26*(3), 479-489. https://doi.org/10.1029/WR026i003p00479

509 Carrassi, A., Bocquet, M., Bertino, L., & Evensen, G. (2018). Data assimilation in the geosciences: An overview of
510 methods, issues, and perspectives. *WIREs Climate Change*, *9*(5), e535. https://doi.org/10.1002/wcc.535

511 Chakraborty, S. (2021). Transfer learning based multi-fidelity physics informed deep neural network. *Journal of*
512 *Computational Physics*, *426*, 109942. https://doi.org/10.1016/j.jcp.2020.109942

513 Chen, G., Luo, X., Jiao, J. J., & Jiang, C. (2023). Fracture network characterization with deep generative model
514 based stochastic inversion. *Energy*, *273*, 127302. https://doi.org/10.1016/j.energy.2023.127302

515 Coleman, T. F., & Li, Y. (1996). An interior trust region approach for nonlinear minimization subject to bounds.
516 *SIAM Journal on Optimization*, *6*(2), 418-445. https://doi.org/10.1137/0806023

517 Djuric, P. M., Kotecha, J. H., Zhang, J., Huang, Y., Ghirmai, T., Bugallo, M. F., & Miguez, J. (2003). Particle
518 filtering. *IEEE Signal Processing Magazine*, *20*(5), 19-38. https://doi.org/10.1109/MSP.2003.1236770

519 Elahi, S. H., & Jafarpour, B. (2018). Dynamic Fracture Characterization From Tracer-Test and Flow-Rate Data With
520 Ensemble Kalman Filter. *SPE Journal*, *23*(2), 449-466. https://doi.org/10.2118/189449-pa

521 Elsheikh, A. H., Wheeler, M. F., & Hoteit, I. (2013). Clustered iterative stochastic ensemble method for multi-modal
522 calibration of subsurface flow models. *Journal of Hydrology*, *491*, 40-55.
523 https://doi.org/10.1016/j.jhydrol.2013.03.037

524 Emerick, A. A., & Reynolds, A. C. (2013). Ensemble smoother with multiple data assimilation. *Computers &*
525 *Geosciences*, *55*, 3-15. https://doi.org/10.1016/j.cageo.2012.03.011

526 Evensen, G. (2009). *Data assimilation: the ensemble Kalman filter*: Springer.

527 Fletcher, S. J. (2022). *Data assimilation for the geosciences: From theory to application*: Elsevier.

528 Godoy, V. A., Napa-García, G. F., & Gómez-Hernández, J. J. (2022). Ensemble random forest filter: An alternative
529 to the ensemble Kalman filter for inverse modeling. *Journal of Hydrology*, *615*, 128642.
530 https://doi.org/10.1016/j.jhydrol.2022.128642

531 Gu, Y., & Oliver, D. S. (2007). An iterative ensemble Kalman filter for multiphase fluid flow data assimilation. *SPE*
532 *Journal*, *12*(4), 438-446. https://doi.org/10.2118/108438-pa

533 Guo, T., Zhang, Y., Zhang, W., Niu, B., He, J., Chen, M., Yu, Y., Xiao, B., & Xu, R. (2022). Numerical simulation
534 of geothermal energy productivity considering the evolution of permeability in various fractures. *Applied Thermal*
535 *Engineering*, *201*, 117756. https://doi.org/10.1016/j.applthermaleng.2021.117756

536 Hyman, J. D. (2020). Flow channeling in fracture networks: characterizing the effect of density on preferential flow
537 path formation. *Water Resources Research*, *56*(9), e2020WR027986. https://doi.org/10.1029/2020WR027986

538 Jiang, C., Niu, B., Yin, G., Zhang, D., Yu, T., & Wang, P. (2019). CT-based 3D reconstruction of the geometry and
539 propagation of hydraulic fracturing in shale. *Journal of Petroleum Science and Engineering*, *179*, 899-911.
540 https://doi.org/10.1016/j.petrol.2019.04.103

Jiang, J., & Younis, R. M. (2017). An improved projection-based embedded discrete fracture model (pEDFM) for multiphase flow in fractured reservoirs. *Advances in Water Resources*, *109*, 267-289. https://doi.org/10.1016/j.advwatres.2017.09.017

Klepikova, M., Brixel, B., & Jalali, M. (2020). Transient hydraulic tomography approach to characterize main flowpaths and their connectivity in fractured media. *Advances in Water Resources*, *136*, 103500. https://doi.org/10.1016/j.advwatres.2019.103500

Koohbor, B., Fahs, M., Hoteit, H., Doummar, J., Younes, A., & Belfort, B. (2020). An advanced discrete fracture model for variably saturated flow in fractured porous media. *Advances in Water Resources*, *140*, 103602. https://doi.org/10.1016/j.advwatres.2020.103602

Li, S., Kang, Z., Feng, X. T., Pan, Z., Huang, X., & Zhang, D. (2020). Three‐dimensional hydrochemical model for dissolutional growth of fractures in karst aquifers. *Water Resources Research*, *56*(3), e2019WR025631. https://doi.org/10.1029/2019WR025631

Li, Y., Hou, J., & Ma, X. (2016). Data integration in characterizing a fracture-cavity reservoir, Tahe oilfield, Tarim basin, China. *Arabian Journal of Geosciences*, *9*, 1-12. https://doi.org/10.1007/s12517-016-2562-z

Lie, K.-A., & Møyner, O. (2021). *Advanced Modeling with the MATLAB Reservoir Simulation Toolbox*. Cambridge, UK: Cambridge University Press.

Lu, L., & Zhang, D. X. (2015). Assisted History Matching for Fractured Reservoirs by Use of Hough-Transform-Based Parameterization. *SPE Journal*, *20*(5), 942-961. https://doi.org/10.2118/176024-Pa

Luo, Z., Xie, Y., Zhao, L., Cheng, L., & Wen, G. (2022). A two‐phase flow extended finite element technology modeling CO2 in fractured porous media. *Greenhouse Gases: Science and Technology*, *12*(6), 712-728. https://doi.org/10.1002/ghg.2182

Man, J., Guo, Y., Jin, J., Zhang, J., Yao, Y., & Zhang, J. (2022). Characterization of vapor intrusion sites with a deep learning-based data assimilation method. *Journal of Hazardous Materials*, *431*, 128600. https://doi.org/10.1016/j.jhazmat.2022.128600

Mariethoz, G., Renard, P., & Straubhaar, J. (2010). The Direct Sampling method to perform multiple-point geostatistical simulations. *Water Resources Research*, *46*(11), W11536. https://doi.org/10.1029/2008wr007621

Miskimins, J. (2009). The importance of geophysical and petrophysical data integration for the hydraulic fracturing of unconventional reservoirs. *The Leading Edge*, *28*(7), 844-849. https://doi.org/10.1190/1.3167787

Moinfar, A., Varavei, A., Sepehrnoori, K., & Johns, R. T. (2014). Development of an efficient embedded discrete fracture model for 3D compositional reservoir simulation in fractured reservoirs. *SPE Journal*, *19*(2), 289-303. https://doi.org/10.2118/154246-PA

Nan, T., & Zhang, J. (2023). Matlab Code of PEDL [Software]. *ResearchGate* https://doi.org/10.13140/RG.2.2.26400.76803

National Academies of Sciences, E., and Medicine (2020). *Characterization, Modeling, Monitoring, and Remediation of Fractured Rock*. Washington, DC: National Academies Press.

Neuman, S. P. (2005). Trends, prospects and challenges in quantifying flow and transport through fractured rocks. *Hydrogeology Journal*, *13*(1), 124-147. https://doi.org/10.1007/s10040-004-0397-2

Ping, J., & Zhang, D. X. (2013). History matching of fracture distributions by ensemble Kalman filter combined with vector based level set parameterization. *Journal of Petroleum Science and Engineering*, *108*, 288-303. https://doi.org/10.1016/j.petrol.2013.04.018

Presho, M., Wo, S., & Ginting, V. (2011). Calibrated dual porosity, dual permeability modeling of fractured reservoirs. *Journal of Petroleum Science and Engineering*, *77*(3-4), 326-337. https://doi.org/10.1016/j.petrol.2011.04.007

Ronneberger, O., Fischer, P., & Brox, T. (2015). U-net: Convolutional networks for biomedical image segmentation. In *Medical Image Computing and Computer-Assisted Intervention–MICCAI 2015: 18th International Conference, Munich, Germany, October 5-9, 2015, Proceedings, Part III 18* (pp. 234-241). Springer.

Saceanu, M. C., Paluszny, A., Zimmerman, R. W., & Ivars, D. M. (2022). Fracture growth leading to mechanical spalling around deposition boreholes of an underground nuclear waste repository. *International Journal of Rock Mechanics and Mining Sciences*, *152*, 105038. https://doi.org/10.1016/j.ijrmms.2022.105038

Shen, C. (2018). A Transdisciplinary Review of Deep Learning Research and Its Relevance for Water Resources Scientists. *Water Resources Research*, *54*(11), 8558-8593. https://doi.org/10.1029/2018wr022643

Sun, A. Y., Morris, A. P., & Mohanty, S. (2009). Sequential updating of multimodal hydrogeologic parameter fields using localization and clustering techniques. *Water Resources Research*, *45*(7), W07424. https://doi.org/10.1029/2008wr007443

Tsang, Y., Tsang, C., Hale, F., & Dverstorp, B. (1996). Tracer transport in a stochastic continuum model of fractured media. *Water Resources Research*, *32*(10), 3077-3092. https://doi.org/10.1029/96WR01397

Viswanathan, H. S., et al. (2022). From Fluid Flow to Coupled Processes in Fractured Rock: Recent Advances and New Frontiers. *Reviews of Geophysics*, *60*(1), e2021RG000744. https://doi.org/10.1029/2021rg000744

Vogt, C., Marquart, G., Kosack, C., Wolf, A., & Clauser, C. (2012). Estimating the permeability distribution and its uncertainty at the EGS demonstration reservoir Soultz‐sous‐Forêts using the ensemble Kalman filter. *Water Resources Research*, *48*(8), W08517. https://doi.org/10.1029/2011WR011673

Vrugt, J. A. (2016). Markov chain Monte Carlo simulation using the DREAM software package: Theory, concepts, and MATLAB implementation. *Environmental Modelling & Software*, *75*, 273-316. https://doi.org/10.1016/j.envsoft.2015.08.013

Wang, Y., & Yan, B. (2022). On the Feasibility of An Ensemble Multi-Fidelity Neural Network for Fast Data Assimilation for Subsurface Flow in Porous Media. *Available at SSRN*. https://doi.org/10.2139/ssrn.4293917

Wu, H., Zhou, Y., Yao, Y., & Wu, K. (2019). Imaged based fractal characterization of micro-fracture structure in coal. *Fuel*, *239*, 53-62. https://doi.org/10.1016/j.fuel.2018.10.117

Wu, H., Fu, P., Hawkins, A. J., Tang, H., & Morris, J. P. (2021). Predicting Thermal Performance of an Enhanced Geothermal System From Tracer Tests in a Data Assimilation Framework. *Water Resources Research*, *57*(12), e2021WR030987. https://doi.org/10.1029/2021wr030987

Xiao, C., Zhang, S., Ma, X., Zhou, T., Hou, T., & Chen, F. (2023). Deep-learning-generalized data-space inversion and uncertainty quantification framework for accelerating geological CO2 plume migration monitoring. *Geoenergy Science and Engineering*, *224*, 211627. https://doi.org/10.1016/j.geoen.2023.211627

Xue, L., Liu, Y., Nan, T., Liu, Q., & Jiang, X. (2020). An efficient automatic history matching method through the probabilistic collocation based particle filter for shale gas reservoir. *Journal of Petroleum Science and Engineering*, *190*, 107086. https://doi.org/10.1016/j.petrol.2020.107086

Yao, M., Chang, H., Li, X., & Zhang, D. (2018). Tuning Fractures With Dynamic Data. *Water Resources Research*, *54*(2), 680-707. https://doi.org/10.1002/2017wr022019

Zhang, F., & Emami-Meybodi, H. (2022). A type-curve method for two-phase flowback analysis in hydraulically fractured hydrocarbon reservoirs. *Journal of Petroleum Science and Engineering*, *209*, 109912. https://doi.org/10.1016/j.petrol.2021.109912

Zhang, J., Zheng, Q., Wu, L., & Zeng, L. (2020). Using Deep Learning to Improve Ensemble Smoother: Applications to Subsurface Characterization. *Water Resources Research*, *56*(12), e2020WR027399. https://doi.org/10.1029/2020wr027399

Zhang, J., Lin, G., Li, W., Wu, L., & Zeng, L. (2018). An Iterative Local Updating Ensemble Smoother for Estimation and Uncertainty Assessment of Hydrologic Model Parameters With Multimodal Distributions. *Water Resources Research*, *54*(3), 1716-1733. https://doi.org/10.1002/2017wr020906

Zhang, J., Cao, C., Nan, T., Ju, L., Zhou, H., & Zeng, L. (2023). A Novel Deep Learning Approach for Data Assimilation of Complex Hydrological Systems. *Authorea Preprints.* https://doi.org/10.22541/essoar.168565409.90872406/v1